Numerical investigation of liquefaction susceptibility of sands considering fabric effects

Bayraktaroglu, H.; González Acosta, J.L.; van den Eijnden, A.P.; Korff, M.; Hicks, M.A.

DOI
10.53243/NUMGE2023-208

Publication date
2023

Document Version
Final published version

Published in
Proceedings 10th NUMGE 2023

Proceedings 10th NUMGE 2023
10th European Conference on Numerical Methods in Geotechnical Engineering
Zdravkovic L, Kontoe S, Taborda DMG, Tsiampousi A (eds)

https://doi.org/10.53243/NUMGE2023-208

Numerical investigation of liquefaction susceptibility of sands considering fabric effects

H. Bayraktaroglu, J.L. González Acosta, A.P. van den Eijnden, M. Korff, M.A. Hicks

Geo-Engineering Section, Faculty of Civil Engineering and Geosciences,
Delft University of Technology, The Netherlands

ABSTRACT: Natural soil deposits may possess a highly anisotropic nature. The fabric anisotropy of soils which is induced during the soil formation process can lead to severe variation in field scale responses. Although the influence of fabric on the response of sands is well known and several advanced constitutive models have been developed to account for it, most of the studies incorporating anisotropy have focused on element test simulations while practical boundary value problem simulations are usually omitted. In this paper, the undrained response and liquefaction resistance of anisotropic sand deposits with different inherent fabric anisotropies are numerically investigated through element test simulations and one-dimensional nonlinear effective stress site response analyses. A novel semi-micromechanical constitutive model accounting for the effect of fabric anisotropy on sand liquefaction has been incorporated into a fully coupled dynamic in-house code employing the *u-p* formulation. The proposed numerical framework shows that, in both element test simulations and site response analyses, the fabric effects stemming from both the inherent and induced anisotropies can significantly influence the liquefaction resistance of sands.

Keywords: Sand; Fabric; Liquefaction; Finite element modelling; Seismic response analysis

1 INTRODUCTION

Anisotropy in sand results in direction-dependent behaviour. Laboratory tests and virtual discrete element simulations show that a change in the orientation of the loading direction may drastically change the sand response, even under the same total stress path. Hollow cylinder torsional shear tests conducted by Nakata et al. (1998) and Yoshimine et al. (1998) show typical examples of loading orientation dependent behaviour. Similar fabric effects have also been encountered in large scale experimental investigations. Azami et al. (2010) and Li et al. (2011) studied the influence of fabric anisotropy on bearing capacity, Yu et al. (2023) investigated the cyclic response of monopiles buried in sands with different deposition angles and Ueda et al. (2019) conducted dynamic centrifuge tests on a liquefiable soil deposit with different inherent anisotropies. These investigations highlight the significant influence of fabric on the mechanical behaviour of sands.

Liquefaction susceptibility and site response analyses (SRA) are fields in which soil inhomogeneities must be considered. This has been partially achieved through implementing advanced constitutive models (Ramirez et al. 2018; Taiebat et al. 2007) and using random field techniques (González Acosta et al. 2022), yet the role of fabric effects has so far been omitted.

In this study, the influence of the initial fabric anisotropy on the liquefaction potential of sands has first been assessed through standard element test simulations, namely cyclic triaxial and simple shear tests, by changing the fabric intensity and orientation (i.e. inherent anisotropy), and then through one-dimensional SRA by changing the initial fabric characteristics.

2 FINITE ELEMENT FORMULATION

To investigate the significance of soil fabric during seismic conditions, a finite element code has been developed incorporating (i) the *u-p* formulation to capture undrained behaviour, (ii) tied degrees (TD) of freedom to simulate the earthquake wave propagation, and (iii) a multilaminate constitutive model to capture anisotropic cyclic behaviour. Regarding the FE formulation, the *u-p* version is selected to simulate undrained behaviour during an earthquake. This formulation is written as,

$$\begin{bmatrix} \mathbf{M} & \mathbf{0} \\ \mathbf{0} & \mathbf{0} \end{bmatrix} \begin{Bmatrix} \mathbf{a} \\ \ddot{\mathbf{p}} \end{Bmatrix} + \begin{bmatrix} \mathbf{0} & \mathbf{0} \\ \mathbf{Q}^{\mathrm{T}} & \mathbf{S} \end{bmatrix} \begin{Bmatrix} \mathbf{v} \\ \dot{\mathbf{p}} \end{Bmatrix} + \begin{bmatrix} \mathbf{K} & -\mathbf{Q} \\ \mathbf{0} & \mathbf{H} \end{bmatrix} \begin{Bmatrix} \mathbf{u} \\ \mathbf{p} \end{Bmatrix} = \begin{Bmatrix} \mathbf{f} \\ \mathbf{0} \end{Bmatrix} \quad (1)$$

where $\mathbf{M}$ and $\mathbf{Q}$ are the mass and hydro-mechanical coupling matrices, respectively, $\mathbf{S}$ and $\mathbf{H}$ are the compressibility and permeability matrices of the pore fluid, respectively, $\mathbf{K}$ is the stiffness matrix of the soil skeleton defined in terms of effective stresses, $\mathbf{a}$, $\mathbf{v}$ and

$\mathbf{u}$ are the vectors of nodal acceleration, velocity and displacement, respectively, $\mathbf{p}$ is the vector of pore water pressure where $\dot{\mathbf{p}}$ indicates time differentiation, and $\mathbf{f}$ is the vector of internal and external forces. A detailed explanation of the *u-p* formulation, including time discretization, can be found in Zienkiewicz et al. (1999). With respect to boundary conditions, TD were implemented by duplicating the degrees of freedom (dof) at both sides of the domain. Figure 1 shows a sketch of a row of square elements considering TD. A detailed explanation of how to implement TD can be found in Cook et al. (1989).

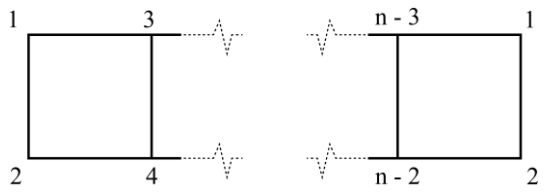

Figure 1. Sketch of tied degrees of freedom

3 CONSTITUTIVE FRAMEWORK

In this paper, the dynamic behaviour of the soil is investigated using the slip theory based on the multilaminate framework. Unlike the classical continuum approach, where constitutive models are used to create a direct link between the stress and strain tensors, in the multilaminate framework local stress and strain vectors are interconnected at so-called sampling planes. The resistance against shearing/sliding and the resultant volumetric changes are calculated individually at each of these sampling planes using proper constitutive formulations.

Although a detailed formulation of the multilaminate framework is beyond the scope of this paper, fundamentals of it together with the constitutive and fabric anisotropy formulations will be provided in the next sections. In the upcoming constitutive formulations, all stresses are effective, so that prime symbols will be omitted, e.g. $p = p'$.

3.1 Multilaminate framework

A statically constrained multilaminate framework consisting of a total of 33×2 orthogonally symmetric sampling planes has been used, at which the traction stress vector components are defined based on the volumetric-deviatoric split method as follows:

$$\boldsymbol{\sigma}_i = \begin{pmatrix} \sigma_n \\ \tau \end{pmatrix} \text{ and } \boldsymbol{\tau} = \begin{pmatrix} s \\ t \end{pmatrix} = \begin{pmatrix} \left(\boldsymbol{\sigma}^* \boldsymbol{n}_i\right) \boldsymbol{n}_s \\ \left(\boldsymbol{\sigma}^* \boldsymbol{n}_i\right) \boldsymbol{n}_t \end{pmatrix} \tag{2}$$

where $\boldsymbol{n}_i$ is the unit normal vector of the i^{th} sampling plane, and $\boldsymbol{\sigma}_i$ is the traction stress vector with local components σ_n, s and t as illustrated in Figure 2. The normal stress component, σ_n, is further decomposed into volumetric and deviatoric parts as $\sigma_n = \sigma_{n,vol} + \sigma_{n,dev}$ with $\sigma_{n,vol} = p$ and $\sigma_{n,dev} = \left(\boldsymbol{\sigma}^* \boldsymbol{n}_i\right) \boldsymbol{n}_i$ where * indicates the deviator part of the tensor.

During shearing, if plasticity is triggered at sampling planes, the resultant local plastic strain increments must be transferred back to their global counterpart $\mathbf{d\varepsilon^p}$, using numerical integration by means of the principle of complementary virtual work over a unit hemisphere, i.e.

$$\mathbf{d\varepsilon^p} = \int_{\Omega} \mathbf{T}_i \mathbf{d}\boldsymbol{\varepsilon}_i^p \, d\Omega \cong 3 \cdot \sum_{i=1}^{33} \mathbf{T}_i \mathbf{d}\boldsymbol{\varepsilon}_i^p w_i \quad \text{with} \quad \sum_{i=1}^{33} w_i = 1.0 \tag{3}$$

where $\mathbf{T}_i$ is the local transformation matrix and w_i is the local weighting coefficient. The above numerical integration follows the work of Carol and Bazant (1997).

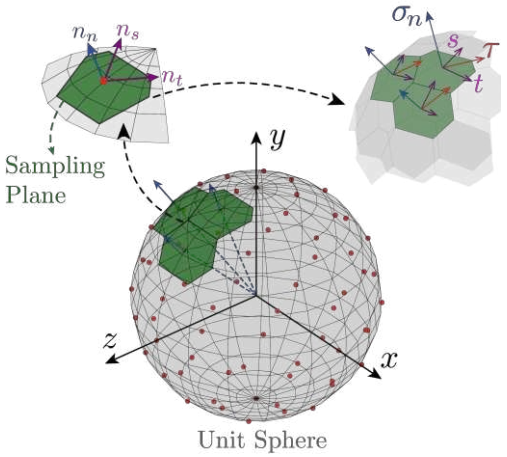

Figure 2. Multilaminate framework and local stresses

The predefined sampling planes (i.e., green polygons) approximating a unit sphere (i.e., an integration point) and the local stress components are illustrated in Figure 2. Due to orthogonal symmetry only the half-space (i.e., 33 sampling planes) is considered. The set of vectors defining the orientation of sampling planes are adopted from Bažant and Oh (1986) and the local shear coordinates $\boldsymbol{n}_s$ and $\boldsymbol{n}_t$ are determined according to Hasegawa and Bažant (1993).

3.2 Constitutive model

In this section, a new state-dependent semi-micromechanical model is described within the framework of anisotropic critical state theory (ACST) proposed by Li and Dafalias (2012). The model builds on the bounding surface plasticity model proposed by Dafalias and Manzari (2004) which will be referred to hereafter as SANISAND04. The schematic of the three characteristic surfaces, namely the bounding, dilatancy and constant volume surfaces, and a yield surface, which

are used to describe constitutive formulations in the subsequent sections are illustrated on a normalised shear plane in Figure 3.

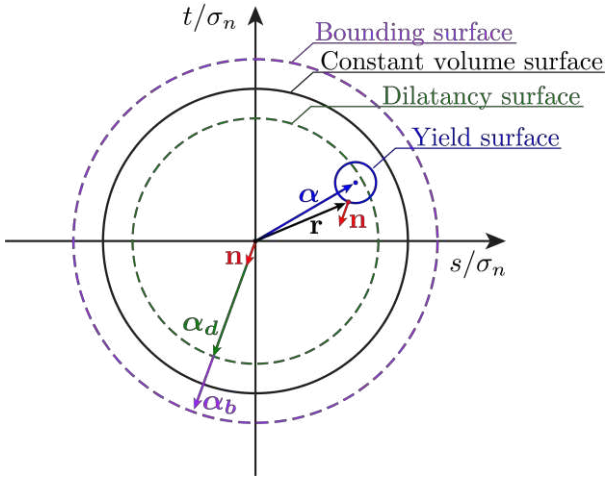

Figure 3. Schematic of the bounding, constant volume, dilatancy and yield surfaces on a normalised shear plane

Even though the shapes of the characteristic surfaces are circles on the normalised shear plane (and cones in local stress space), their resultant global counterparts produced by the multilaminate framework intrinsically includes Lode angle dependency.

From here on, for simplicity, the subscript i denoting the sampling plane will be omitted. Unless stated otherwise, all constitutive formulations can be assumed to be defined at the sampling planes.

3.2.1 Multilaminate adaptation

The tensorial formulations and constitutive terms in SANISAND04 should be downscaled to their vectorial counterparts to be used in the multilaminate framework. In this regard, the definitions of some of the key constitutive ingredients have been changed and these are redefined in this section.

In the proposed constitutive model, the back-stress ratio vector $\boldsymbol{\alpha}$ and the stress ratio vector $\mathbf{r}$ generalise the slope of the yield surface and stress ratio, respectively, on the normalised shear plane. The loading direction vector $\mathbf{n}$ used to define the direction of the image back-stress ratios is derived as $\mathbf{n}=(\mathbf{r}-\boldsymbol{\alpha})/|\mathbf{r}-\boldsymbol{\alpha}|$, where $\mathbf{n}$ is normal to the yield surface. Note that all these local quantities whose components are defined in the n_s and n_t directions are vectors and will be utilized to define the constitutive formulations in the next section.

3.2.2 Summary of constitutive model formulation

The basic formulations used to describe the proposed constitutive model are categorised in Table 1. Instead of discussing each individual constitutive formulation in Equations (4-15), the following key points are highlighted:

- Although the concept of the bounding surface employed in this work is the same as in SANISAND04, the critical state void ratio formulation in Equation (6) and variables f_b and f_d which are used to scale the local bounding and dilatancy surfaces in Equations (8-9), are adopted from Wan and Guo (1998).
- The positive factor h in Equation (7) is adopted from the work of Petalas et al. (2020) to include the influence of fabric on the plastic hardening modulus.
- Plastic flow in the shear plane is determined using the normality rule; however, plastic flow normal to the sampling planes is governed by the stress-dilatancy formulation given in Equation (10).
- For simplicity, similar to other ACST based constitutive models, all fabric formulations are defined in global tensorial space. A multilaminate specific implementation of the ACST with sampling plane level local fabric formulations can be found in Bayraktaroglu et al. (2023a) and Bayraktaroglu et al. (2023b).
- Finally, note that the global unit-norm deviatoric plastic strain rate direction tensor $\mathbf{n}'$ in Equations (13-14) differs from the loading direction vector $\mathbf{n}$. This is crucial for properly capturing fabric effects upon a loading reversal.

Table 1. Constitutive model formulations

Category	Formulation	
Yield surface	$f=\left[(\mathbf{r}-\boldsymbol{\alpha}):(\mathbf{r}-\boldsymbol{\alpha})\right]^{1/2}-m$	(4)
Elasticity	$G=G_0 p_{at}\dfrac{(2.97-e)^2}{1+e}\left(\dfrac{p}{p_{at}}\right)^{0.5}$	(5)
Critical state	$e_c=e_{c,0}\exp\left(-\left(\dfrac{p}{h_s}\right)^n\right)$	(6)
Plastic modulus	$h=\dfrac{G_0 h_0\exp(A_{fab})(1/e-c_h)^2}{(\boldsymbol{\alpha}-\boldsymbol{\alpha}_{in}):\mathbf{n}}\left(\dfrac{p_{at}}{\sigma_n}\right)^{0.5}$	(7)
Bounding surface	$\alpha_b=f_b M-m$ and $f_b=(e/e_d)^{-\alpha}$	(8)
Dilatancy surface	$\alpha_d=f_d M-m$ and $f_d=(e/e_d)^{\beta}$	(9)
Dilatancy	$d=A_d(\boldsymbol{\alpha}_d-\boldsymbol{\alpha}):\mathbf{n}$	(10)
	$A_d=A_0(1+\langle \mathbf{z}\mathbf{n}\rangle)$	(11)
	$d\mathbf{z}=-c_z\langle -d\varepsilon_n^p\rangle(z_{\max}\mathbf{n}+\mathbf{z})$	(12)
Fabric	$A_{fab}=\mathbf{F}:\mathbf{n}'$	(13)
	$\dot{\mathbf{F}}=k_{fab}\exp(A_{fab})(\mathbf{n}'-\mathbf{F})\lvert\dot{\varepsilon}_q^p\rvert$	(14)
Dilatancy state	$e_d=e_c+e_A(A_{fab}-1)$	(15)

4 RESULTS

Even though different laboratory sample preparation methods create different inherent fabric anisotropies, they provide limited control over the initial microstructural arrangement, so that experimental data cannot be used for validation purposes since they cannot ensure the relevant inherent fabric anisotropy information. Hence, in this paper, a hypothetical sand with the material parameters listed in Table 2 have been used, both for the element test simulations and the site response analyses. The detailed calibration procedure for the model parameters can be found in Bayraktaroglu et al. (2023b). Values of $F_{in}=0.0$ and $F_{in}=0.5$ have been selected to define initially isotropic and anisotropic fabric structures, respectively. In addition to F_{in}, the influence of the orientation of the initial fabric tensor has been investigated by rotating the fabric tensor by an angle θ_{in} according to orthogonal transformation. Finally, in order to facilitate direct comparisons, a void ratio of 0.8 has been used both in the element test and SRA simulations.

Table 2. Constitutive model parameters

Category	Parameter	Value
Elasticity	G_0	125
	ν	0.15
Critical state	M	1.2
	h_s	20000
	n	0.74
	$e_{c,0}$	0.934
Yield surface	m	0.017
Plastic modulus	h_0	7.0
	c_h	0.95
	α	2
Dilatancy	A_0	0.6
	β	3
	$z_{\max}$	4.0
	c_z	600
Fabric	e_A	0.05
	F_{in}	0.0 and 0.5
	k_{fab}	5.0

4.1 *Element test simulations*

In this section, the influence of the fabric intensity and orientation on the undrained cyclic shear strength, i.e. liquefaction resistance, of sands is assessed through standard element test simulations.

In Figure 4, undrained cyclic triaxial test simulations with three different initial fabric arrangements are compared. The initially anisotropic configurations, indicated with green and red lines, result in lower liquefaction resistance than the initially isotropic case which is indicated by a blue line. Moreover, more plastic strains accumulate in both anisotropic cases compared to their isotropic counterpart. The difference between the two anisotropic cases arises from their different initial fabric orientations.

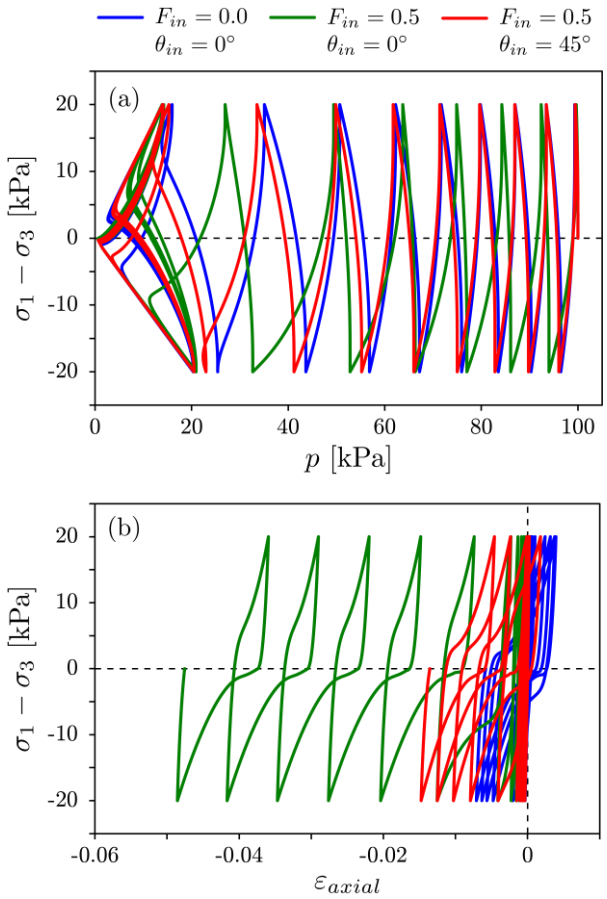

Figure 4. Influence of the fabric intensity and orientation on sand behaviour in undrained cyclic triaxial test

In Figure 5, three different cyclic undrained simple shear test simulations are compared. Again, the initially anisotropic simulation indicated with the red line requires fewer cycles to reach liquefaction and yields significantly more accumulated plastic strain compared to the initially isotropic case indicated by the blue line. However, unlike Figure 4, the initially anisotropic simulation indicated by the green line does not yield a noticeable difference. This is due to the relative orientation between the loading and fabric tensors. Refering to Equation (13), at the begining of shearing, the simulation represented by blue yields $A_{fab}=0$ since $F_{in}=0$ and also the anisotropic simulation indicated by green line yields $A_{fab}=0$ since the loading and fabric directions are orthogonal to each other. The limited fabric evolution due to the small loading amplitudes hinders the difference between these two simulations.

Note that the biased plastic strain accumulations and the one way ratcheting at the post-liquefaction state in

Figure 4b and 5b are shortcomings of SANISAND04. However, these can be improved by employing the concept of semifluidized state proposed by Barrero et al. (2020). Detailed comparisons of these, and other limitations of bounding surface models together with other advanced models, can be found in Duque et al. (2022).

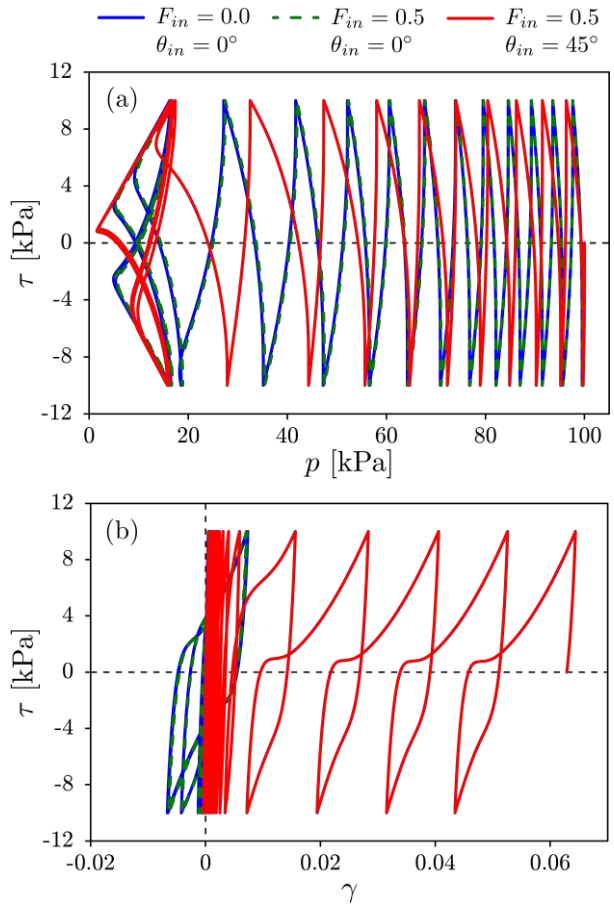

Figure 5. Influence of the fabric intensity and orientation on sand behaviour in undrained cyclic simple shear test

4.2 Site response analysis

To investigate the repercussions of incorporating fabric effects in a liquefiable soil, an SRA is proposed considering the following conditions. A one-dimensional column of 10 m height with a water table located at 1 m depth is subjected to a seismic load taken from the 1987 Superstition Hills earthquake. The initial field stresses are determined assuming $K_0 = 0.5$. The schematic of the FE model is presented in Figure 6.

Two identical SRAs with different initial fabric configurations, i.e., initially isotropic and anisotropic, have been carried out and the contours of $r_u = \Delta u / \sigma'_{v0}$, where Δu is the increment of water pore pressure and σ'_{v0} is the initial effective stress, are presented in Figure 6. In both simulations, the maximum value of r_u, which indicates the zone susceptible to liquefaction, is reached at a depth of 2.2 m. However, similar to observations in element test simulations, the initially anisotropic fabric structure yielded a lower liquefaction resistance, i.e. a higher value of r_u, throughout the analysis.

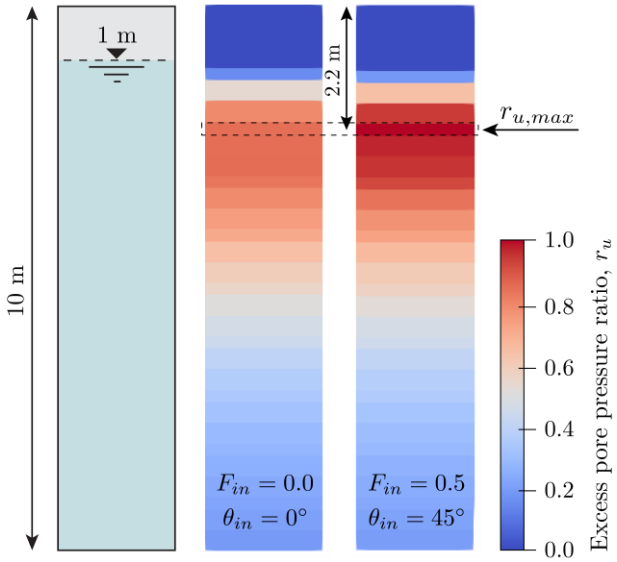

Figure 6. Contours of r_u at the end of the earthquake

A detailed comparison of the excess pore pressure accumulations at the $r_{u,\max}$ depth is presented in Figure 7. Similar to observations in the element test simulations, the initially anisotropic fabric structure yielded a lower liquefaction resistance, i.e. a faster excess pore pressure accumulation and a higher value of $r_{u,\max}$.

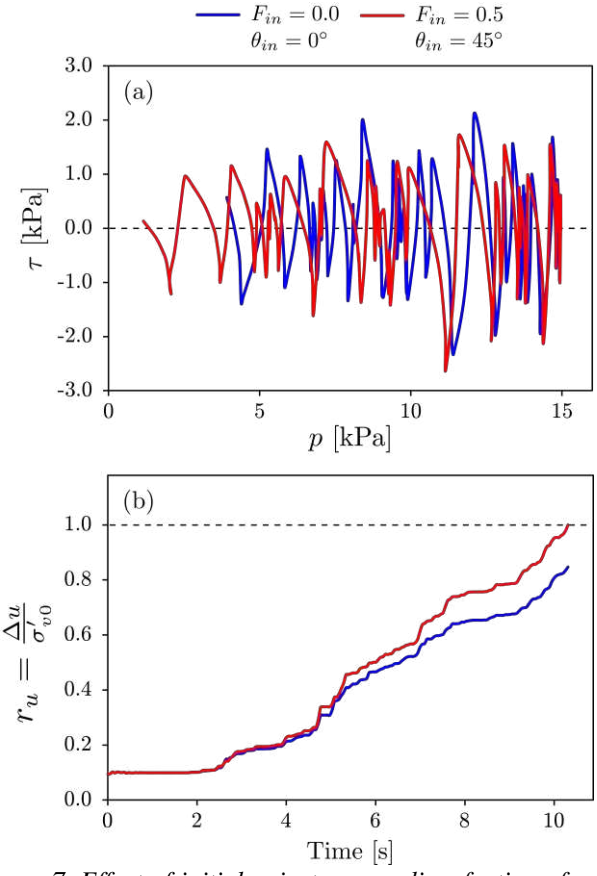

Figure 7. Effect of initial anisotropy on liquefaction of sand at 2.2 m depth

5 CONCLUSION

A novel semi-micromechanical constitutive formulation for anisotropic sands has been proposed, and the influence of the initial fabric anisotropy on the liquefaction resistance of sands has been investigated through element test simulations and field scale dynamic site response analyses. Results indicate that the initial fabric anisotropy may cause significant variation in soil response. The element test simulations show that, rather than solely the intensity of the anisotropy, its relative orientation with respect to the loading direction controls the system behaviour. Furthermore, an isotropic idealization of soil may lead to underestimating the liquefaction potential and ground response.

6 ACKNOWLEDGEMENTS

The activity presented in the paper is part of the research programme DeepNL/SOFTTOP with project number DEEP.NL.2018.006, financed by the Netherlands Organisation for Scientific Research (NWO).

7 REFERENCES

Azami, A., Pietruszczak, S., and Guo, P. 2010. Bearing capacity of shallow foundations in transversely isotropic granular media. *International Journal for Numerical and Analytical Methods in Geomechanics*, 34(8), 771-793.

Barrero, A. R., Taiebat, M., and Dafalias, Y. F. 2020. Modeling cyclic shearing of sands in the semifluidized state. *International Journal for Numerical and Analytical Methods in Geomechanics*, 44(3), 371-388.

Bayraktaroglu, H., Hicks, M. A., and Korff, M. 2023. A Semi-micromechanical Framework for Anisotropic Sands. *Challenges and Innovations in Geomechanics*, Springer International Publishing, Cham, 63-70.

Bayraktaroglu, H., Hicks, M. A., Korff, M., and Galavi, V. 2023. A state-dependent multilaminate constitutive model for anisotropic sands. *Géotechnique*, doi: 10.1680/jgeot.22.00165.

Bažant, P., and Oh, B. 1986. Efficient numerical integration on the surface of a sphere. *ZAMM-Journal of Applied Mathematics and Mechanics/Zeitschrift für Angewandte Mathematik und Mechanik*, 66(1), 37-49.

Carol, I., and Bazant, Z. P. 1997. Damage and plasticity in microplane theory. *International Journal of Solids and Structures*, 34(29), 3807-3835.

Cook, R. D., Malkus, D. S., and Plesha, M. E. 1989. *Concepts and applications of finite element analysis*, John Wiley & Sons, New York.

Dafalias, Y., and Manzari, M. 2004. Simple plasticity sand model accounting for fabric change effects. *Journal of Engineering Mechanics*, 130(6), 622-634.

Duque, J., Yang, M., Fuentes, W., Mašín, D., and Taiebat, M. 2022. Characteristic limitations of advanced plasticity and hypoplasticity models for cyclic loading of sands. *Acta Geotechnica*, 17(6), 2235-2257.

González Acosta, J., van den Eijnden, A., and Hicks, M. 2022. Comparison of 1D and 2D liquefaction assessment methods considering soil spatial variability. *Proc., 8th International Symposium on Geotechnical Safety and Risk (ISGSR)*.

Hasegawa, T., and Bažant, Z. P. 1993. Nonlocal microplane concrete model with rate effect and load cycles. I: general formulation. *Journal of Materials in Civil Engineering*, 5(3), 372-393.

Li, B., Zeng, X., and Yu, H. 2011. Effect of fabric anisotropy on seismic response of strip foundations. *GeoRisk 2011*, 326-335.

Li, X. S., and Dafalias, Y. F. 2012. Anisotropic critical state theory: role of fabric. *Journal of Engineering Mechanics*, 138(3), 263-275.

Nakata, Y., Hyodo, M., Murata, H., and Yasufuku, N. 1998. Flow deformation of sands subjected to principal stress rotation. *Soils and Foundations*, 38(2), 115-128.

Petalas, A. L., Dafalias, Y. F., and Papadimitriou, A. G. 2020. SANISAND-F: Sand constitutive model with evolving fabric anisotropy. *International Journal of Solids and Structures*, 188-189, 12-31.

Ramirez, J., Barrero Andres, R., Chen, L., Dashti, S., Ghofrani, A., Taiebat, M., and Arduino, P. 2018. Site Response in a Layered Liquefiable Deposit: Evaluation of Different Numerical Tools and Methodologies with Centrifuge Experimental Results. *Journal of Geotechnical and Geoenvironmental Engineering*, 144(10), 04018073.

Taiebat, M., Shahir, H., and Pak, A. 2007. Study of pore pressure variation during liquefaction using two constitutive models for sand. *Soil Dynamics and Earthquake Engineering*, 27(1), 60-72.

Ueda, K., Uratani, K., and Iai, S. 2019. Influence of inherent anisotropy on the seismic behavior of liquefiable sandy level ground. *Soils and Foundations*, 59(2), 458-473.

Wan, R. G., and Guo, P. J. 1998. A simple constitutive model for granular soils: modified stress-dilatancy approach. *Computers and Geotechnics*, 22(2), 109-133.

Yoshimine, M., Ishihara, K., and Vargas, W. 1998. Effects of principal stress direction and intermediate principal stress on undrained shear behavior of sand. *Soils and Foundations*, 38(3), 179-188.

Yu, F., Zhang, C., Huang, M., Yang, X., and Yao, Z. 2023. Model Tests on Cyclic Responses of a Laterally Loaded Pile Considering Sand Anisotropy and Scouring. *Journal of Marine Science and Engineering*.

Zienkiewicz, O. C., Chan, A. H. C., Pastor, M., Schrefler, B. A., and Shiomi, T. 1999. *Computational geomechanics with special reference to earthquake engineering*, John Wiley & Sons, Chichester ; New York.